

1 Pressurizing magma within heterogeneous crust: a case 2 study at the Socorro Magma Body, New Mexico, USA

3 Grant A. Block¹, Mousumi Roy¹, Emily Graves², Ronni Grapenthin²

4 ¹Department of Physics and Astronomy, University of New Mexico, 210 Yale Blvd NE, Albuquerque,
5 87131, NM, USA.

6 ²Geophysical Institute and Department of Geoscience, University of Alaska, 2156 Koyukuk Drive,
7 Fairbanks, 99775, AK, USA.

8 This manuscript is under review at *Geophysical Review Letters* and has not com-
9 pleted the revision process.

10 Key Points:

- 11 • InSAR confirms coeval subsidence and uplift (a so-called “sombbrero” deformation
12 pattern) persisted for >100 years at the Socorro Magma Body
- 13 • A compliant region, modeled as a viscoelastic body surrounding a sill, is able to
14 reproduce both the pattern and duration of deformation.
- 15 • Viscoelastic deformation within a broad compliant region supports the presence
16 of mush zones at SMB and other mid-crustal magma bodies.

Corresponding author: Grant A. Block, gblock@unm.edu

Abstract

Surface deformation plays a key role in illuminating magma transport at active volcanoes, however, unambiguous separation of deep and shallow transport remains elusive. The Socorro Magma Body (SMB) lacks an upper crustal magma transport system, allowing us to link geodetic measurements with predictions of numerical models investigating rheologic heterogeneities and magma-mush interaction in the mid-/lower crust. New InSAR observations confirm that a pattern of central surface uplift surrounded by a region of subsidence (previously coined “sombbrero” deformation) has persisted over >100 yrs at the SMB. Our models suggest this pattern may reflect the presence of a large (>100 km width), weaker-than-ambient, compliant region (CR) surrounding the mid-crustal magma body. Interactions between a pressurizing (e.g., due to melt injection and/or volatile exsolution) sill-like magma body and CR drive the sombrero pattern, depending on both viscoelastic relaxation and pressurization timescales, explaining its rare observation and transient nature.

Plain Language Summary

Magma in the crust is transported and stored within magma bodies (regions that are mostly liquid magma) and “mush” (mostly solid crystals and some liquid magma). Mush zones are thought to be too viscous to be erupted but are likely to be weaker than the surrounding rock. To understand volcanic eruptions, it is important to understand the distribution of magma and mush, and their mutual interactions. Here we study these interactions in a mid-crustal magma body, the Socorro Magma Body (SMB), that does not have a surface volcano. Surface deformation at the SMB helps us study magma-mush interaction, especially in the middle or lower crust. Previous surface deformation measurements at the SMB show “sombbrero” deformation: a central area of uplift surrounded by a ring of subsidence. New satellite radar measurements are consistent with the previously reported pattern, confirming that this deformation remained remarkably constant through nearly 100 years. We suggest this is due to a large weak, mush region surrounding the SMB. Our computer models reproduce a long-lasting, consistent sombrero deformation pattern depending on mush properties as well as pressurization history of the magma body, and we suggest these factors may explain why this pattern is relatively rare.

1 Introduction

Long-lived active volcanic centers are the uppermost expression of a complex transcrustal transport system bringing magma from beneath and within the lithosphere to the surface (e.g., Hildreth & Wilson, 2007; Cashman et al., 2017). These systems comprise partially molten regions, thought to be a combination of crystal-poor magma bodies surrounded by crystal-rich “mush” zones near solidus (Cooper & Kent, 2014; Glazner et al., 2016; Jackson et al., 2018). Mush zones, where crystal volume fractions exceed 50-60%, are thought to be deformable but not readily eruptible (e.g., A. Costa et al., 2009; Bachmann & Bergantz, 2008). Within them, the formation of crystal-poor (< 50% crystals by volume) eruptible magma (e.g., Hughes et al., 2021) by heat and mass transfer is the subject of multidisciplinary exploration (e.g., F. Costa et al., 2020; Bergantz et al., 2015). Magma-mush interactions have been modeled as (visco)poroelastic coupling over length scales of intrusions (Mullet & Segall, 2022; Liao et al., 2018, 2021; Alshembari et al., 2023), or permeable flow and transport (Liu & Lee, 2021), possibly including the effects of volatiles (e.g., Parmigiani et al., 2014).

Mush zones in the upper crust are well documented at a number of active volcanic centers (e.g., Hamling et al., 2015), however, the role of mush in the mid-/lower crust is poorly understood (Annen et al., 2006; Maguire et al., 2022; Magee et al., 2018). For example, seismic observations at two large and dynamic mid-crustal magma bodies, the Socorro Magma Body (SMB) and the Altiplano-Puna Magma Body (APMB), suggest a broad (>100 km wide; e.g., Fig. 1a) region of anomalously low seismic wavespeeds in the mid-crust (Ward et al., 2014; Pritchard & Gregg, 2016; Gao et al., 2004; West et al., 2004; Wilson et al., 2005). These seismic anomalies coincide with volcanism (e.g., at the APMB, Long Valley, or Yellowstone) or elevated surface heatflow (e.g., Reiter et al., 2010), anomalous resistivity structure (e.g., Comeau et al., 2015), and anomalous seismicity (Sanford et al., 2002; Jay et al., 2012; Hudson et al., 2022; Rinehart & Sanford, 1981; Stankova et al., 2008), suggesting they are thermally/mechanically anomalous. While these regional mid-crustal seismic anomalies are consistent with the presence of melt (Maguire et al., 2022; Magee et al., 2018; Ake & Sanford, 1988), we lack an understanding of how magma and mush may be distributed within them and what role they play in the larger transcrustal magma transport system. For example, the APMB underlies numerous volcanoes (Magee et al., 2018; Gottsmann et al., 2017) and it is not clear how magma and mush are distributed within it. Thermal modeling of episodic melt injection suggests prolonged

80 heating is necessary to generate long-lived mush zones (Annen et al., 2015; Blundy &
 81 Annen, 2016; Karakas et al., 2017). Such mush zones are likely weaker than the surround-
 82 ing crust (Diener & Fagereng, 2014), but the implications of the resulting rheologic het-
 83 erogeneity have not been fully considered in studies of surface deformation due to pres-
 84 surizing mid-crustal magma bodies.

85 Inspired by regionally-extensive mid-crustal seismic anomalies, we use numerical
 86 models to study the role of spatial (horizontal and vertical) heterogeneity within the mid-
 87 crust in controlling the surface deformation response to mid-crustal magma pressuriza-
 88 tion. We are interested in the mechanical coupling between a mid-crustal compliant re-
 89 gion (CR) and a pressurizing sill-like magma body. Separating surface deformation pat-
 90 terns due to mid-crustal magma injection and shallower magma dynamics proves diffi-
 91 cult where the magma transport system extends to a volcanic system (e.g., Uturuncu
 92 Volcano, Long Valley, or Yellowstone) as upper crustal deformation obscures deeper pro-
 93 cesses (Biggs & Pritchard, 2017). The SMB (Fig. 1), a large, seismically inferred, sill-
 94 like magma body at 19 km depth (diameter 50-70 km and thickness <1 km; Rinehart
 95 & Sanford, 1981; Balch et al., 1997; Fialko et al., 2001), does not have a volcanic ex-
 96 pression. We exploit this lack of upper crustal magma transport at the SMB to directly
 97 connect geodetic observations to mid-crustal drivers of deformation.

98 Our starting point is a pattern of central uplift surrounded by subsidence, so-called
 99 “sombbrero uplift” (coined by Fialko & Pearse, 2012), observed above both the SMB (Larsen
 100 et al., 1986; Pearse & Fialko, 2010; Fialko & Pearse, 2012; Finnegan & Pritchard, 2009)
 101 and the APMB at Uturuncu volcano (Fialko & Pearse, 2012; Henderson & Pritchard,
 102 2017; Gottsmann et al., 2018). For the APMB this deformation has been modeled as de-
 103 formation that couples magma injection at depth with either deeper crustal mechanics
 104 (Fialko & Pearse, 2012; Henderson & Pritchard, 2017), or the dynamics of a shallow upper-
 105 crustal mush zone (Gottsmann et al., 2017). The SMB, however, lacks an upper crustal
 106 expression of the magma transport system motivating the question of how such a som-
 107brero pattern might arise and what impact the presence of a CR may have.

108 A key finding of our study is that a mid-crustal CR surrounding the SMB leads
 109 to a spatial decoupling of surface deformation. Generally, vertical surface uplift directly
 110 above a pressurizing sill-like body (radius r_{source}) within a CR may be accompanied by
 111 surface subsidence of regions toward the edges of the CR ($r \gtrsim 1.5r_{source}$), providing an

112 alternative mechanism for emergence of the sombrero pattern. The transient nature of
 113 the sombrero pattern and its duration ($\Delta\tau_{som}$) is a strong function of the rheologic gra-
 114 dients within the CR and the pressure-time history within the sill, providing an expla-
 115 nation for its rare observation. Importantly, the surface expression of the deformation
 116 is controlled by the interplay of the pressurization timescale and the effective (viscoelas-
 117 tic) response timescale in the CR.

118 **2 Deformation observations at the Socorro Magma Body**

119 At the SMB, the sombrero pattern of surface motion has been measured over nearly
 120 100 years through leveling (Larsen et al., 1986) and Interferometric Synthetic Aperture
 121 Radar (InSAR) (Fialko et al., 2001; Pearse & Fialko, 2010). These observations, together
 122 with other geodetic measurements (Berglund et al., 2012; Larsen et al., 1986), suggest
 123 a maximum vertical uplift rate of $\approx 2\text{-}2.5$ mm/yr.

124 We acquire Synthetic Aperture Radar (SAR) observations on ascending path 49
 125 frame 107 (Fig. 1b), collected by the European Space Agency’s Sentinel-1 A/B mission
 126 (Torres et al., 2012), which we process with GMTSAR (Sandwell et al., 2011) to create
 127 2 pass interferograms spanning January 2017 through December 2021. We create mean
 128 velocity stacks (supplementary text S1) from individual interferograms which include De-
 129 cember through January multi-year pairs by averaging the observed line-of-sight (LOS)
 130 deformation over the time interval of acquisition where observations are weighed by the
 131 time interval (e.g., Xiao et al., 2020). The resulting LOS velocity field (Fig. 1b), aligned
 132 with prior observations (Pearse & Fialko, 2010; Finnegan & Pritchard, 2009; Fialko et
 133 al., 2001) to fit the magnitude of observations, reveals deformation overlying the SMB.
 134 From the average LOS deformation map (Fig. 1b), we extract profiles for comparison
 135 to our SMB-specific finite-element model results (Fig 5c). We observe ≈ 3 mm/yr of peak
 136 LOS uplift within the SMB, with uplift limited to the central to western portion of the
 137 magma body. North-south and east-west profiles across the peak deformation illustrate
 138 the sombrero uplift over the magma body as described by Pearse and Fialko (2010). While
 139 residual topography impacts may bias the velocity field, we do not observe similar ef-
 140 fects over other nearby topography.

141 Previous InSAR observations over the SMB report deformation rates of 2-3 mm/yr
 142 (Pearse & Fialko, 2010; Finnegan & Pritchard, 2009; Fialko et al., 2001), comparable to

143 our observations during the duration of the SAR acquisitions. We observe a north-south
 144 elongated region of uplift, more consistent with Fialko et al. (2001) than the circular de-
 145 formation shown by Finnegan and Pritchard (2009). Temporal changes in the InSAR-
 146 derived average LOS velocities over the SMB were presented in Finnegan and Pritchard
 147 (2009), therefore, variations in the shape of the region experiencing uplift during our study
 148 are not unprecedented.

149 This deformation signal is generally attributed to injection of magma in the mid-
 150 crust, however, many studies suggest it cannot be due to solely elastic effects (e.g., Fi-
 151 alko et al., 2001; Pearse & Fialko, 2010; Fialko & Pearse, 2012). Previous models of de-
 152 formation at the SMB (Larsen et al., 1986; Fialko et al., 2001; Pearse & Fialko, 2010;
 153 Finnegan & Pritchard, 2009; A. Newman et al., 2001; A. V. Newman et al., 2006) do not
 154 explicitly consider material heterogeneity in a mid-crustal CR, the main target of our
 155 investigation.

156 **3 Numerical Modeling Results**

157 We present generic finite element models using PyLith (v2.2.2; Aagaard et al., 2017),
 158 to assess the role of a CR surrounding a sill-like pressure source in the mid-crust. We
 159 target the role of the CR and its manifestation in ground deformation (parameters and
 160 model details in supplementary text S2, Table S1, and Fig. S1). Each model comprises
 161 a background layered structure, with deformation driven by time-varying pressurization
 162 of a mid-crustal sill (Fig. 2b). We consider a suite of models, with and without a vis-
 163 coelastic CR surrounding the sill, and explore the effects of varying CR structure (Fig.
 164 2a; Table S1).

165 A viscoelastic CR in the mid-crust (with lower viscosity than the ambient viscoelas-
 166 tic crust), leads to a phase-lag in surface deformation. When the sill within the CR un-
 167 dergoes pressurization, regions above its center and those to its edges (e.g., $r \geq 1.5r_{source}$)
 168 may be out of phase (demonstrated for vertical motions in Fig 3a and for horizontal mo-
 169 tions in Fig S3). This is the essence of the sombrero signal (central uplift surrounded by
 170 an annular moat of subsidence), and we observe this pattern during the (re-)pressurization
 171 phase (Fig. 2b), where the center begins to uplift while the edges are still subsiding due
 172 to viscoelastic relaxation of the CR. The sombrero pattern is only observed in the pres-

173 ence of a CR (Fig. 3a); without it, surface velocities are in phase everywhere and have
 174 the same sign (Fig 3b).

175 When a CR exists, surface motions above the source (within $r/r_{source} \leq 1$) and out-
 176 side it ($r/r_{source} \gtrsim 1.5$) depend on: (1) rheologic gradients within the CR and (2) the ap-
 177 plied pressurization history (Fig. 3c-f). Depending on the gradient of viscosity within
 178 the CR, we observe a circulatory pattern of motion in the mid-crust (e.g., Fig. 2d,e) and
 179 a phase lag between vertical surface velocities above the sill (“center”) and outside of
 180 the source radius (“shoulder”; Fig. 3c-f; see also Fig S2). The time interval when ver-
 181 tical velocities at the center are positive and the shoulder regions are subsiding is the
 182 sombrero duration, $\Delta\tau_{som}$ (and vice versa, for a “reverse” sombrero, e.g., Fig 3d).

183 Spatial decoupling of the center and shoulder velocities during sombrero deforma-
 184 tion depends on the rheologic gradient within the CR: comparing uniform CR model vs
 185 models with horizontal (“nested”) and vertical (“stacked”) viscosity gradients (Fig. 2a).
 186 A larger CR viscosity gradient increases the phase lag compared to the uniform CR mod-
 187 els (Fig. S2b, d), with systematically higher phase lags in the nested CR model than the
 188 stacked CR model (Fig. S2). Horizontal viscosity gradients are, therefore, more impor-
 189 tant than vertical ones for controlling sombrero-style deformation.

190 In addition to rheologic gradients, the phase lag in surface velocities is strongly con-
 191 trolled by the pressure-time function. Sinusoidal pressure-time functions yield periodic
 192 motions where $\Delta\tau_{som}$ corresponds to a fixed (phase- and) time-lag for both the sombrero
 193 and the reverse sombrero (Fig. 3c,d,f). For sawtooth pressurization, however, the du-
 194 ration of the sombrero may greatly exceed that of the reverse pattern (Fig. 3e). Nested
 195 CR models driven by sawtooth pressurization (Fig. 3e) exhibit near-constant surface ve-
 196 locities during a sombrero event.

197 Decreasing the pressurization rate (e.g., $dP/dt \approx 4\Delta P/T$ for the sinusoidal func-
 198 tion) leads to increased sombrero duration, $\Delta\tau_{som}$ (Fig. 4). The sombrero duration $\Delta\tau_{som}$
 199 for a given $\Delta P/T$ increases with the ambient background pressure, P_0 , and decreases with
 200 relaxation time t_r (Fig 4a). For the uniform CR, the relation between $\Delta\tau_{som}$ and $\Delta P/T$
 201 collapses into a single trend when the duration is normalized by the uniform relaxation
 202 time within the CR, t_r , and the pressurization rate is normalized by P_0/t_r (Fig. 4b). Nested
 203 and stacked CR runs also collapse onto similar trends showing an increase in $\Delta\tau_{som}$ at
 204 low $\Delta P t_r / P_0 T$, with systematically higher sombrero durations compared to the uniform

205 CR models at the same dimensionless pressurization rate (Fig. 4b). (We use a volumetrically-
 206 averaged relaxation time to nondimensionalize in non-uniform CRs). For the uniform
 207 and stacked CR models, there is a transition at low $\Delta Pt_r/P_0T$ at which the sombrero
 208 duration is not as sensitive to the pressurization rate. The slope of the trend is similar
 209 for nested CR models, but without a similar observed transition at low rates. (Reach-
 210 ing a dimensionless pressurization rate of $\Delta Pt_r/P_0T=10^{-2}$ is computationally expen-
 211 sive for the nested and stacked CR models due to the large volumetrically-averaged t_r .)
 212 The uniform and stacked CR models clearly reach a threshold at which $\Delta\tau_{som}$ appears
 213 to be nearly independent of $\Delta Pt_r/P_0T$, suggesting the threshold depends on intra-CR
 214 rheology ($\Delta Pt_r/P_0T\approx 10^{-2}$ for uniform CR and 10^{-1} for stacked CR; Fig. 4b). Mod-
 215 els with the same pressurization rate but different pressure-time functions show little vari-
 216 ation in sombrero duration, demonstrating that the primary controlling factors for som-
 217 brero duration are the pressurization rate and model geometry, and not pressure-time
 218 history (Fig. 4).

219 4 Discussion

220 While idealized, the generic models above demonstrate that a weaker-than-ambient
 221 CR surrounding a (de-)pressurizing sill can decouple surface deformation directly above
 222 the sill from points farther away. A key finding is that, during pressurization, locations
 223 vertically above the sill may be uplifting while those outside the surface projection of
 224 the sill may be subsiding, creating a sombrero pattern (Fig. 3). (The pattern may be
 225 reversed when transitioning to a period of de-pressurization.) This phase lag in the sur-
 226 face deformation pattern depends on the presence of the CR, but the duration of the som-
 227 brero depends primarily on pressurization rate: increasing with decreasing pressuriza-
 228 tion rate, up to a threshold (Fig. 4). Strong viscosity gradients paired with asymmet-
 229 ric pressurization lead to long sombrero durations with nearly steady ground motions
 230 (Fig. 3e and Fig. 4b). Crucially, a long period of re-pressurization (with roughly con-
 231 stant dP/dt) followed by a sudden decrease in pressure results in a sombrero that lasts
 232 longer than the reverse-sombrero, with slowly-varying surface velocities during the som-
 233 brero (Fig. 3d). Although we lack constraints on SMB sill pressures, rheologic proper-
 234 ties of anatexites suggest that the the bulk strength of partially-molten rocks in the mid-
 235 dle or lower crust range from $\leq 1-5$ MPa during cycles of melt production and drainage
 236 (Diener & Fagereng, 2014). The range of background pressures, P_0 , and pressure changes

237 ΔP , in our models (Fig. 4) is consistent with expectations for weakened partially molten
 238 crustal mineralogies (Diener & Fagereng, 2014).

239 We now present an SMB-specific model constrained by seismic and geodetic ob-
 240 servations discussed above: (1) a sill-like body at ≈ 19 km depth, elliptical in mapview,
 241 surrounded by anomalously low V_s in the mid-crust (Balch et al., 1997; Rinehart & San-
 242 ford, 1981; West et al., 2004, Fig 1a); and (2) a long-lived ($\Delta\tau_{som} \geq 100$ yrs) sombrero
 243 pattern of deformation, with nearly constant surface motions (Fialko et al., 2001; Pearse
 244 & Fialko, 2010; Finnegan & Pritchard, 2009; Larsen et al., 1986, Fig. 1). Assuming that
 245 the V_s anomaly $\leq 5\%$ at ≈ 20 km depth region in West et al. (2004) is a proxy for a weaker-
 246 than-ambient CR (dashed yellow circle in Fig 1b), we specify horizontal and vertical gra-
 247 dients in CR viscosity (see Table S1). The 200 km diameter of the hybrid CR follows
 248 the extent of the low-velocity mid-crustal V_s anomaly and the sill-like ellipsoidal source
 249 has thickness 1 km and mapview radii of 24 and 38 km (Fig 5a). With this geophysically-
 250 informed SMB-model, we explore the background pressure P_0 needed to match the am-
 251 plitude of the InSAR LOS observations and the pressurization rate dP/dt needed to gener-
 252 ate a long-lived (>100 yr) sombrero pattern.

253 We find that a sill pressurized to a background pressure of $P_0=1.0$ MPa, with a con-
 254 stant pressure increase of $dP/dt=4\Delta P/T=5$ kPa/yr (implemented as a sawtooth pressure-
 255 time function with $\Delta P=250$ kPa and $T=200$ yrs; Fig 5b), produces a reasonable fit to
 256 the InSAR observations (A-A' and B-B' in Fig. 5c). The modeled sombrero duration of
 257 $\Delta\tau_{som}=148$ yrs is characterized by persistent, nearly steady surface motions for over 100
 258 yrs, comparable to long-term observations at the SMB (Fig.5c). The width of the mod-
 259 eled deformation depends on the seismically-constrained geometry, and no further ad-
 260 justment was used to fit the width of the surface pattern in Fig. 5c.

261 The inferred pressurization rate of $dP/dt \approx 5$ kPa/yr (comparable to Pearse & Fi-
 262 alko, 2010) may be interpreted as due to injection of magma, or to pressurization due
 263 to volatile degassing. If driven by magma injection alone, we infer a volumetric rate $dV/dt =$
 264 $\beta V_0(dP/dt)$ where β is the magma compressibility and V_0 is an initial volume. Compress-
 265 ibility of a gas-poor, basaltic magma at 19 km depth is likely lower than compressibil-
 266 ity above 10 km depth (e.g., $\beta \approx 0.4 - 2 \times 10^{-10}$ Pa $^{-1}$; Rivalta and Segall (2008)), so
 267 $\beta = 0.4 \times 10^{-10}$ Pa $^{-1}$ is a reasonable upper bound. Following pressurization to $P_0 \approx 1$
 268 MPa, the initial volume of the ellipsoidal source (Table S1) is ≈ 1940 km 3 , so $dV/dt \approx$

269 $3.88 \times 10^{-4} \text{ km}^3/\text{yr}$. On the other hand, if the source of pressurization includes exsolved
 270 volatiles, this inferred volumetric injection rate is likely an overestimate. A dry (≤ 0.2
 271 wt % H_2O) basaltic magma (e.g., expected in a rift-setting) with ≥ 4000 ppm CO_2 at
 272 $\geq 1000^\circ\text{C}$ is likely to reach saturation at pressures above 500 MPa, comparable to con-
 273 ditions at 19 km depth within the Rio Grande Rift. We lack direct constraints on the
 274 CO_2 content of the SMB, however, mantle xenoliths from the nearby Rio Puerco and Kil-
 275 bourne Hole Volcanic Fields have undergone metasomatism by carbonatitic fluids (Porreca
 276 & Selverstone, 2006; Harvey et al., 2012), suggesting that CO_2 -rich fluids may be abun-
 277 dant in the SMB. Therefore, the inferred pressurization above may be due to a combi-
 278 nation of gas exsolution together with magma injection, but we lack constraints on the
 279 relative roles of these processes.

280 Observations at the APMB span a shorter timeframe than the SMB, and suggest
 281 a peak uplift rate at Uturuncu Volcano of $\approx 0.5\text{-}1 \text{ cm/yr}$ (Fialko & Pearce, 2012; Hen-
 282 derson & Pritchard, 2017; Gottsmann et al., 2018). Here, 50 years of geodetic observa-
 283 tions suggest transient sombrero deformation (Fialko & Pearce, 2012; Eiden et al., 2023;
 284 Gottsmann et al., 2018), and our models provide an explanation for this transience. The
 285 inferred pressurization rate at the SMB ($\approx 5 \text{ kPa/yr}$) is smaller than modeled beneath
 286 Uturuncu if all of the deformation is ascribed to upper crustal processes (Gottsmann et
 287 al., 2017). As we have demonstrated, for a given pressurization rate the duration of the
 288 sombrero pattern is controlled by decoupling between surface motions within $r < 1.5r_{source}$
 289 and $r \geq 1.5r_{source}$, and this decoupling and phase lag depends on intra-CR viscosity gra-
 290 dients (Fig S2). Specifically, sombrero durations will be smaller (and therefore manifest
 291 their transience over shorter timescales) if the mid-crustal CR is uniform in rheology vs.
 292 if it has significant rheologic gradients within it (Figs 4; S2). Our models raise the pos-
 293 sibility that at least part of the transient sombrero pattern in the APMB may indeed
 294 be attributed to lateral heterogeneity in the mid-crust, with perhaps a more rheologi-
 295 cally uniform CR than in the SMB.

296 While these results make a compelling case for the role of a weaker-than-ambient
 297 CR in the SMB geodetic signal, our models cannot differentiate between thermal weak-
 298 ening and the presence of mush within the CR. Thermoelastic effects have been inferred
 299 for driving deformation at active volcanoes (Masterlark & Lu, 2004; Furuya, 2005; Wang
 300 & Aoki, 2019). A simple inversion for thermoelastic drivers requires both heating and
 301 cooling sources deeper than the SMB (see text S3). We suggest therefore that thermoe-

302 lasticity is unlikely to be a primary driver of surface uplift in the region. Additionally,
303 we acknowledge important complexities are ignored in our models, e.g., near-surface hy-
304 drology and groundwater extraction (likely due to agriculture is evident at the south-
305 ern end of profile B-B' in Fig 5c, which crosses from the Socorro Basin into the Jornada
306 del Muerto Basin). We also ignore extensional stress and material heterogeneity asso-
307 ciated with the Rio Grande Rift. In future work, we hope to include heat transfer and
308 poro(visco)-elastic effects to more fully explore CR heterogeneity and implications for
309 magma-mush interactions. During time-variable pressurization in the sill, as magma is
310 either sourced from deeper levels or drained from a mush, we might expect time-dependent
311 rheology in the CR as explored in Liao et al. (2021, 2018); Mullet and Segall (2022); Al-
312 shembari et al. (2023). These studies explore interactions in a single melt injection/withdrawal
313 event, however, our models highlight the importance of cyclic pressure-time variations,
314 especially when a CR is present, in decoupled surface deformation. As shown by Liao
315 et al. (2021), two important time scales for controlling stress transfer and surface defor-
316 mation include a short time scale driven by poroelastic diffusion, and a longer viscoelas-
317 tic relaxation time scale. Indeed, the fast depressurization in the sawtooth function may
318 be a proxy for porous diffusion of magma into the surrounding CR mush zone, causing
319 depressurization at a significantly faster rate than allowed by viscous relaxation. Over
320 longer timescales, however, poroviscoelastic effects may be less important than the vis-
321 cous relaxation behavior captured in our models (text S3). Specifically, viscous creep within
322 a weaker-than-ambient mid-crustal CR (e.g., a regionally-extensive partial melt-rich mush)
323 and intra-CR rheologic gradients drive transient surface deformations as seen in the som-
324 brero pattern.

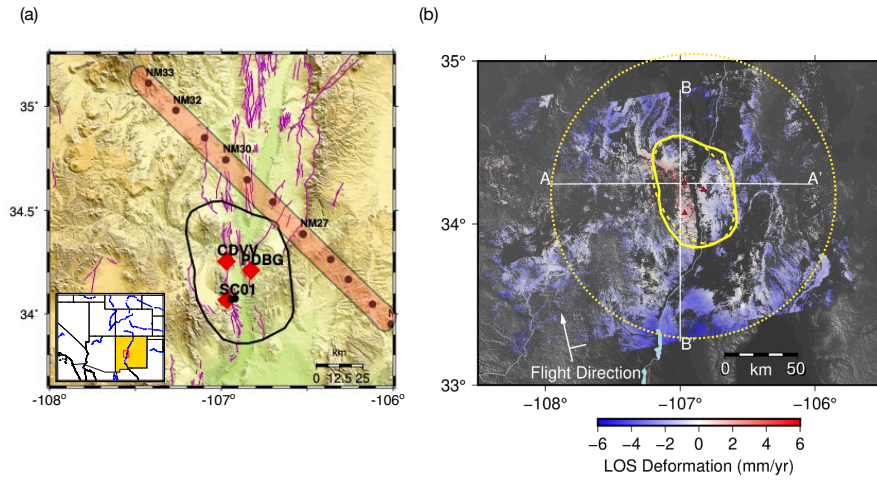


Figure 1. a) Topographic relief map of the seismically derived extent of the Socorro Magma Body (SMB), New Mexico, (Rinehart & Sanford, 1981; Balch et al., 1997), within southwestern North America (inset). Quaternary faults (magenta lines), three continuous GPS stations (red diamonds), and locations of the La Ristra seismic stations (black dots) (West et al., 2004) indicated for reference. The orange polygon outlines the NW-SE extent of low mid-crustal seismic wavespeeds ($\Delta V_s < 5\%$ at ≈ 20 km depth, from (West et al., 2004)). (b). InSAR measurements of the SMB spanning 01/07/2017 through 12/21/2021 showing the observed sombrero-style surface deformation. GPS stations (red) and the SMB outline (solid yellow) are as in (a). The yellow ellipse (long-dashes) outlines the pressure source and the larger yellow circle (short-dashes) shows the map-extent of the CR in the SMB-realistic model (Fig. 5).

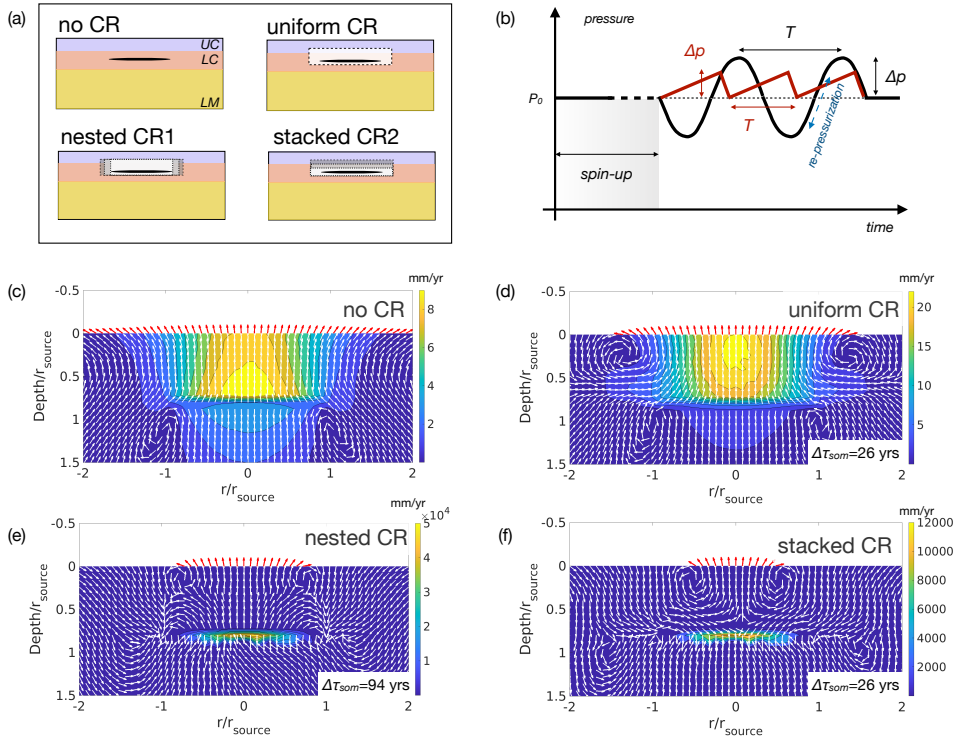


Figure 2. (a) Cross-section cartoons of generic models with variable CR. All models share a layered background rheology (UC=upper crust, LC=lower crust, LM=lithospheric mantle; see S2), within which a mid-crustal pressure source is embedded (black ellipse). The CR rheology is specified with a single viscosity (uniform CR) or with horizontal gradient in nested cylinders (nested CR) or vertical gradient in stacked cylinders (stacked CR). The nested CR viscosity increases radially and the stacked CR has viscosity increasing vertically. (b) After initial pressurization to a background pressure P_0 , followed by a prescribed “spin-up” time at constant pressure, one of two periodic pressure functions is applied: a sinusoid with amplitude ΔP and period T (black), or sawtooth with pressure change ΔP and period T (red). The “re-pressurization” phase of a given pressure-time function refers to intervals with $dP/dt > 0$ as indicated (blue dashed arrows). (c)-(f) Cross sections illustrating spatially-varying velocity (arrows) for models with the same $r_{source} = 25$ km, $P_0 = 1$ MPa, $\Delta P = 500$ kPa and $T = 200$ yrs, (with sinusoidal pressurization), but with differing CR: (c) no CR, (d) a uniform CR, (e) nested CR, and (f) stacked CR. Velocity snapshots are shown halfway during the sombrero (d-f; durations indicated) or halfway through a pressure cycle (c). Arrows show velocity direction; red arrows indicate upward surface motions and color contours indicate velocity magnitude (mm/yr). Note the color bar range is different for each subplot.

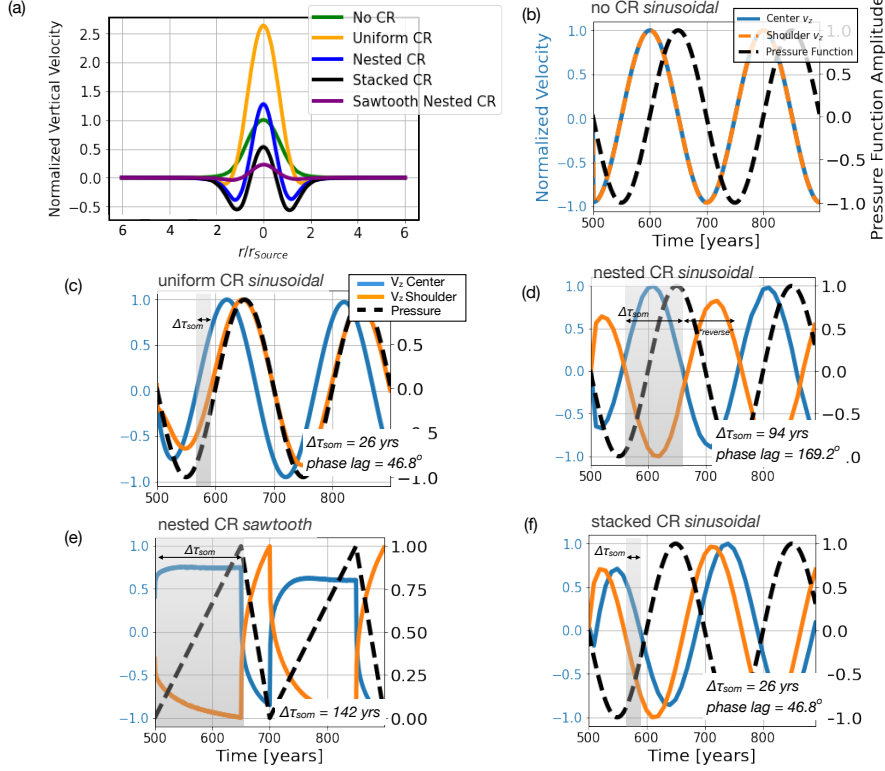


Figure 3. (a) Normalized vertical surface velocity, V_z , profiles (normalized relative to the maximum velocity of the no CR case), illustrating the role of the CR in the sombrero pattern of deformation in four models with varying CR; all with $P_0=1\text{MPa}$, $\Delta P=500\text{kPa}$ and $T=200\text{yrs}$. Each profile is shown at the same times as the corresponding velocity fields in Fig. 2c-f; see Fig S3 for corresponding radial motions. (b)-(d): Normalized surface uplift velocities at the center ($r=0$ km, blue) and shoulder (defined as $r/r_{source}=1.6$, orange), with normalized sinusoidal pressure-time variation (black dashed lines); y-axis labels for (c-f) are as indicated on (b). (b) no CR (corresponds to model in Fig. 2c), (c) a uniform CR (model in Fig. 2d), and (d) nested CR (model in Fig. 2e). (e)-(f) show decoupled center and shoulder velocities for the (e) nested CR and (f) stacked CR driven by pressurization functions as indicated.

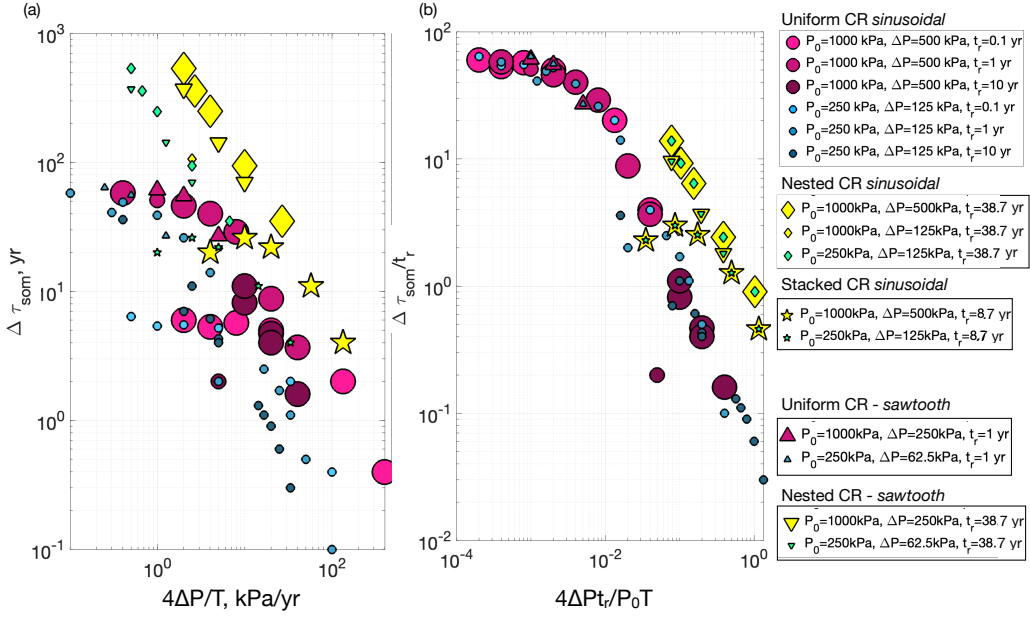


Figure 4. (a) Sombrero duration as a function of pressurization rate for the suite of models in this study. (b) Dimensionless sombrero duration (normalized by CR relaxation time) vs dimensionless pressurization rate (normalized by background pressure and CR relaxation time). In (a) and (b), we see a general trend of increasing sombrero duration with decreasing pressurization rate, up to a threshold. Nondimensionalization collapses all uniform CR runs into a single trend, and likewise with the nested CR and stacked CR models. To normalize nested CR and stacked CR runs, t_r was found by volumetrically averaging the relaxation times within the CR.

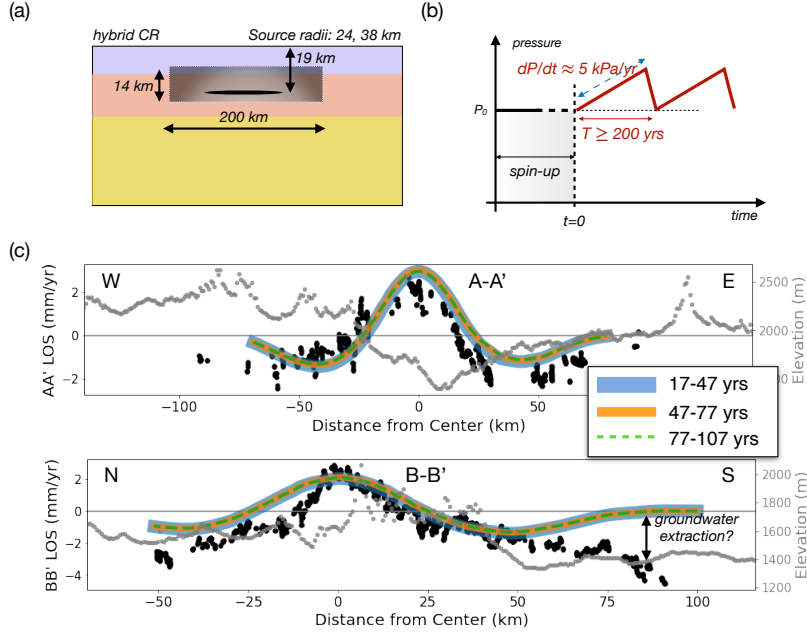


Figure 5. Summary of SMB-realistic ellipsoidal source/hybrid CR model (Table S1) and results. (a) Cartoon schematic illustrating the CR (200 km diameter), with both horizontal and vertical gradients in t_r (represented by the shading moving away from the pressure source (black); Table S1). (b) Sketch of pressure-time function, with constant pressurization at $dP/dt \approx 5 \text{ kPa/yr}$, leading to a nearly stationary sombrero pattern over $\Delta t_{som} > 100 \text{ yrs}$ (sawtooth period $T \geq 200 \text{ yrs}$). (c) Predicted surface velocity profiles (solid and dashed lines) extracted along lines A-A' and B-B' in Fig 1b, projected onto the LOS and averaged over 30 yr windows as indicated ($t=0$ is defined at the beginning of the sawtooth function in (b)). Lines extracted from the model are offset by 10.0 km west and 0.5 km north and rotated by -22.55° . InSAR LOS velocities along profiles A-A' and B-B' (black dots) and topography (light gray dots) are plotted for comparison. The data were converted from degrees to km with the factor $1^\circ \approx 93 \text{ km}$. The misfit at the southern end of the B-B' profile is likely due to groundwater extraction from local agricultural activity.

5 Open Research

All PyLith input files and InSAR data will be made available at the following github repository: <https://github.com/GrantBlock/SMB.FiniteElementModels> and Zenodo (Block, 2023). The PyLith software is freely available at (Aagaard et al., 2017).

Acknowledgments

GB and MR thank: the UNM Center for Advanced Research Computing, supported in part by the National Science Foundation, for resources used in this work; Eric Lindsey for fruitful InSAR discussions; and David Wilson and Mike West for information regarding the La Ristra seismic experiment. MR thanks Emmanuel Codillo for discussions on the magma saturation pressures during the CIDER 2023 workshop. This work was completed while GB was partly supported by NSF EAR-2120812; GB also thanks the CONVERSE network for discussions which helped inform and contextualize this project. EG and RG acknowledge NASA funding through LNIP #80NSSC20K0073. Copernicus Sentinel data 2016-2020. Retrieved from ASF DAAC, processed by ESA.

References

- Aagaard, B., Knepley, M., & Williams, C. (2017). *Pyolith v2.2.2 [software]*. Davis, CA. doi: <http://doi.org/10.5281/zenodo.438705>
- Ake, J., & Sanford, A. (1988). New evidence for the existence and internal structure of a thin layer of magma at mid-crustal depths near Socorro, New Mexico. *Bulletin of the Seismological Society of America*, 78, 1335–1359. doi: 10.1785/BSSA0780031335
- Alshembari, R., Hickey, J., Williamson, B. J., & Cashman, K. (2023). Unveiling the rheological control of magmatic systems on volcano deformation: The interplay of poroviscoelastic magma-mush and thermo-viscoelastic crust. *Journal of Geophysical Research: Solid Earth*, 128(7), e2023JB026625. Retrieved from <https://agupubs.onlinelibrary.wiley.com/doi/abs/10.1029/2023JB026625> (e2023JB026625 2023JB026625) doi: <https://doi.org/10.1029/2023JB026625>
- Annen, C., Blundy, J. D., Leuthold, J., & Sparks, R. S. J. (2015). Construction and evolution of igneous bodies: Towards an integrated perspective of crustal magmatism. *Lithos*, 230, 206–221. doi: <https://doi.org/10.1016/>

356 j.lithos.2015.05.008

357 Annen, C., Blundy, J. D., & Sparks, R. S. J. (2006). The genesis of intermediate
358 and silicic magmas in deep crustal hot zones. *Journal of Petrology*, *47*, 505–
359 539. doi: 10.1093/petrology/egi084

360 Bachmann, O., & Bergantz, G. (2008). The magma reservoirs that feed supererup-
361 tions. *Elements*, *4*, 17-21. doi: 10.2113/GSELEMENTS.4.1.17

362 Balch, R. S., Hartse, H. E., Sanford, A. R., & wan Lin, K. (1997). A new map of the
363 geographic extent of the socorro mid-crustal magma body. *Bulletin of the Seis-
364 mological Society of America*, *87*(1), 174-182.

365 Bergantz, G. W., Schleicher, J. M., & Burgisser, A. (2015). Open-system dynamics
366 and mixing in magma mushes. *Nature Geoscience*, *8*, 793–796. doi: 10.1038/
367 ngeo2534

368 Berglund, H. T., Sheehan, A. F., Murray, M. H., Roy, M., Lowry, A. R., Nerem,
369 R. S., & Blume, F. (2012). Distributed deformation across the rio grande
370 rift, great plains, and colorado plateau. *Geology*, *40*(1), 23-26. doi:
371 10.1130/G32418.1

372 Biggs, J., & Pritchard, M. E. (2017, 02). Global Volcano Monitoring: What Does
373 It Mean When Volcanoes Deform? *Elements*, *13*(1), 17-22. Retrieved from
374 <https://doi.org/10.2113/gselements.13.1.17> doi: 10.2113/gselements.13
375 .1.17

376 Block, G. (2023, August). *Grant-Block/SMB_FiniteElementModels:SMBFiniteElement*
377 *Models [software]*. Zenodo. Retrieved from [https://doi.org/10.5281/
378 zenodo.8212788](https://doi.org/10.5281/zenodo.8212788) doi: 10.5281/zenodo.8212788

379 Blundy, J. D., & Annen, C. J. (2016). Crustal magmatic systems from the perspec-
380 tive of heat transfer. *Elements*, *12*(2), 115–120. doi: [https://doi.org/10.2113/
381 gselements.12.2.115](https://doi.org/10.2113/gselements.12.2.115)

382 Cashman, K. V., Sparks, R. S. J., & Blundy, J. D. (2017). Vertically extensive and
383 unstable magmatic systems: A unified view of igneous processes. *Science*, *355*,
384 1280. doi: 10.1126/science.aag3055

385 Comeau, M. J., Unsworth, M. J., Ticona, F., & Sunagua, M. (2015). Magnetotelluric
386 images of magma distribution beneath volcan uturuncu, bolivia: Implications
387 for magma dynamics. *Geology*, *34*(243-246). doi: 10.1130/G36258.1

388 Cooper, K. M., & Kent, A. J. R. (2014). Rapid remobilization of magmatic crystals

- 389 kept in cold storage. *Nature*, 506(480-483). doi: 10.1038/nature12991
- 390 Costa, A., Caricchi, L., & Bagdassarov, N. (2009). A model for the rheology of
391 particle-bearing suspensions and partially molten. *Geochemistry Geophysics*
392 *Geosystems*, 10(Q03010). doi: 10.1029/2008GC002138
- 393 Costa, F., Shea, T., & Ubide, T. (2020). Diffusion chronometry and the
394 timescales of magmatic processes. *Nature Reviews Earth and Environ-*
395 *ment*. Retrieved from <https://doi.org/10.1038/s43017-020-0038-x> doi:
396 10.1038/s43017-020-0038-x
- 397 Diener, J. F. A., & Fagereng, Å. (2014). The influence of melting and melt drainage
398 on crustal rheology during orogenesis. *Journal of Geophysical Research, Solid*
399 *Earth*, 119, 6193–6210. doi: 10.1002/2014JB011088
- 400 Eiden, E., MacQueen, P., Henderson, S., & Pritchard, M. E. (2023). Multiple spatial
401 and temporal scales of deformation from geodetic monitoring point to active
402 transcrustal magma system at uturuncu volcano, bolivia. *Geosphere*, 19(X),
403 1-13. doi: 10.1130/GES02520.1
- 404 Fialko, Y., & Pearce, J. (2012). Sombbrero uplift above the altiplano-puna magma
405 body: Evidence of a ballooning mid-crustal diapir. *Science*, 338(6104), 250–
406 252. doi: 10.1126/science.1226358
- 407 Fialko, Y., Simons, M., & Khazan, Y. (2001). Finite source modelling of magmatic
408 unrest in socorro, new mexico, and long valley, california. *Geophysical Journal*
409 *International*, 146(1), 191–200. doi: 10.1046/j.1365-246X.2001.00453.x
- 410 Finnegan, N., & Pritchard, M. (2009). Magnitude and duration of surface uplift
411 above the socorro magma body. *Geology*, 37(3), 231-234. Retrieved from
412 <https://doi.org/10.1130/G25132A.1> doi: 10.1130/G25132A.1
- 413 Furuya, M. (2005). Quasi-static thermoelastic deformation in an elastic half-space:
414 theory and application to insar observations at izu-oshima volcano, japan.
415 *Geophysical Journal International*, 161(1), 230–242.
- 416 Gao, W., Grand, S., Baldrige, W. S., Wilson, D., West, M., Ni, J., & Aster, R.
417 (2004). Upper mantle convection beneath the central Rio Grande rift imaged
418 by P and S wave tomography. *Journal of Geophysical Research*, 109. doi:
419 10.1029/2003JB002743
- 420 Glazner, A., Bartley, J., & Coleman, D. (2016). We need a new definition for
421 "magma". *EOS*, 97. doi: 10.1029/2016EO059741

- 422 Gottsmann, J., Blundy, J., Henderson, S., Pritchard, M., & Sparks, R. (2017).
423 Thermomechanical modeling of the altiplano-puna deformation anomaly: Mul-
424 tiparameter insights into magma mush reorganization. *Geosphere*, *13*(4), 1-24.
425 doi: 10.1130/GES01420.1
- 426 Gottsmann, J., delPetro, R., & Muller, C. (2018). 50 years of steady ground defor-
427 mation in the altiplano-puna region of southern bolivia. *Geosphere*, *14*(1), 65-
428 73. doi: 10.1130/GES01570.1.
- 429 Hamling, I. J., Hreinsdottir, S., & Fournier, N. (2015). The ups and downs of the
430 tvz: geodetic observations of deformation around the taupo volcanic zone, new
431 zealand. *Journal of Geophysical Research: Solid Earth*, *120*, 4667–4679. doi:
432 10.1002/2015JB012125.
- 433 Harvey, J., Yoshikawa, M., Hammond, S. J., & Burton, K. W. (2012). Decipher-
434 ing the trace element characteristics in kilbourne hole peridotite xenoliths:
435 Melt-rock interaction and metasomatism beneath the rio grande rift, sw usa.
436 *Journal of Petrology*, *53*(8), 1709-1742.
- 437 Henderson, S. T., & Pritchard, M. E. (2017, 10). Time-dependent deformation of
438 Uturuncu volcano, Bolivia, constrained by GPS and InSAR measurements
439 and implications for source models. *Geosphere*, *13*(6), 1834-1854. doi:
440 10.1130/GES01203.1
- 441 Hildreth, W., & Wilson, C. J. N. (2007). Compositional zoning of the bishop tuff.
442 *Journal of Petrology*, *48*(5). doi: 10.1093/petrology/egm007
- 443 Hudson, T. S., Kendall, J.-M., Pritchard, M. E., Blundy, J. D., & Gottsmann,
444 J. H. (2022). From slab to surface: Earthquake evidence for fluid migra-
445 tion at uturuncu volcano, bolivia. *Earth and Planetary Science Letters*,
446 *577*. Retrieved from <https://doi.org/10.1016/j.epsl.2021.117268> doi:
447 10.1016/j.epsl.2021.117268
- 448 Hughes, G. E., Petrone, C. M., Downes, H., Varley, N. R., & Hammond, S. J.
449 (2021). Mush remobilisation and mafic recharge: A study of the crystal cargo
450 of the 2013–17 eruption at volcán de colima, mexico. *Journal of Volcanology
451 and Geothermal Research*, *416*. doi: 10.1016/j.jvolgeores.2021.107296
- 452 Jackson, M. D., Blundy, J., & Sparks, R. S. J. (2018). Chemical differentiation, cold
453 storage and remobilization of magma in the earth's crust. *Nature*, *564*, 405-
454 409. doi: 10.1038/s41586-018-0746-2

- 455 Jay, J. A., Pritchard, M. E., West, M. E., Christensen, D., Haney, M., Minaya, E.,
456 ... Zabala, M.
- 457 Shallow seismicity, triggered seismicity, and ambient noise tomography at the
458 long-dormant uturuncu volcano, bolivia. . doi: 10.1007/s00445-011-0568-7
- 459 Karakas, O., Degruyter, W., Bachmann, O., & Dufek, J. (2017, Jun 01). Lifetime
460 and size of shallow magma bodies controlled by crustal-scale magmatism. *Nature*
461 *Geoscience*, 10(6), 446-450. Retrieved from [https://doi.org/10.1038/](https://doi.org/10.1038/ngeo2959)
462 [ngeo2959](https://doi.org/10.1038/ngeo2959) doi: 10.1038/ngeo2959
- 463 Larsen, S., Reilinger, R., & Brown, L. (1986). Evidence of ongoing crustal de-
464 formation related to magmatic activity near socorro, new mexico. *Journal*
465 *of Geophysical Research: Solid Earth*, 91(B6), 6283–6292. doi: 10.1029/
466 [JB091iB06p06283](https://doi.org/10.1029/JB091iB06p06283)
- 467 Liao, Y., Soule, S. A., & Jones, M. (2018). On the mechanical effects of poroelastic
468 crystal mush in classical magma chamber models. *Journal of Geophysical Re-*
469 *search*, 123(11). doi: 10.1029/2018JB015985
- 470 Liao, Y., Soule, S. A., Jones, M., & Le Mével, H. (2021). The mechanical response
471 of a magma chamber with poroviscoelastic crystal mush. *Journal of Geophysi-*
472 *cal Research*, 126(4). doi: 10.1029/2020JB019395
- 473 Liu, B., & Lee, C.-T. (2021). Fast melt expulsion from crystal-rich mushes via in-
474 duced anisotropic permeability. *Earth and Planetary Science Letters*, 571. Re-
475 trieved from <https://doi.org/10.1016/j.epsl.2021.117113> doi: 10.1016/
476 [j.epsl.2021.117113](https://doi.org/10.1016/j.epsl.2021.117113)
- 477 Magee, C., Stevenson, C. T., Ebmeier, S. K., Keir, D., Hammond, J. O., Gotts-
478 mann, J. H., ... Jackson, M. D. (2018). Magma plumbing systems: A
479 geophysical perspective. *Journal of Petrology*, 59(6), 1217–1251. doi:
480 [10.1093/petrology/egy064](https://doi.org/10.1093/petrology/egy064)
- 481 Maguire, R., Schmandt, B., Li, J., Jiang, C., Li, G., Wilgus, J., & Chen, M. (2022).
482 Magma accumulation at depths of prior rhyolite storage beneath yellowstone
483 caldera. *Science*, 378, 1001–1004. doi: 10.1126/science.ade0347
- 484 Masterlark, T., & Lu, Z. (2004). Transient volcano deformation sources imaged with
485 interferometric synthetic aperture radar: Application to seguan island, alaska.
486 *Journal of Geophysical Research: Solid Earth*, 109(B1).

- 487 Mullet, B., & Segall, P. (2022). The surface deformation signature of a transcrustal,
488 crystal mush-dominant magma system. *Journal of Geophysical Research*, *127*.
489 doi: 10.1029/2022JB024178
- 490 Newman, A., Dixon, T. H., Ofoegbu, G., & Dixon, J. E. (2001). Geodetic and
491 seismic constraints on recent activity at long valley caldera, california: ev-
492 idence for viscoelastic rheology. *Journal of Volcanology and Geothermal*
493 *Research*, *105*(3), 183–206. doi: [https://doi-org.libproxy.unm.edu/10.1016/](https://doi-org.libproxy.unm.edu/10.1016/S0377-0273(00)00255-9)
494 [S0377-0273\(00\)00255-9](https://doi-org.libproxy.unm.edu/10.1016/S0377-0273(00)00255-9)
- 495 Newman, A. V., Dixon, T. H., & Gourmelen, N. (2006). A four-dimensional vis-
496 coelastic deformation model for long valley caldera, california, between 1995
497 and 2000. *Journal of Volcanology and Geothermal Research*, *150*(1-3), 244–
498 269. doi: <https://doi.org/10.1016/j.jvolgeores.2005.07.017>
- 499 Parmigiani, A., Huber, C., & Bachmann, O. (2014). Mush microphysics and the re-
500 activation of crystal-rich magma reservoirs. *Journal of Geophysical Research*,
501 *119*, 6308–6322. doi: 10.1002/2014JB011124
- 502 Pearse, J., & Fialko, Y. (2010, 07). Mechanics of active magmatic intraplate in
503 the rio grande rift near socorro, new mexico. *Journal of Geophysical Research*,
504 *115*. doi: 10.1029/2009JB006592
- 505 Porreca, C., & Selverstone, J. (2006). Pyroxenite xenoliths from the rio puerco
506 volcanic field, new mexico: Melt metasomatism at the margin of the rio grande
507 rift. *Geosphere*, *2*(7), 333–351;.
- 508 Pritchard, M. E., & Gregg, P. M. (2016). Geophysical evidence for silicic crustal
509 melt in the continents: Where, what kind, and how much? *Elements*, *12*(2),
510 121–127. doi: 10.2113/gselements.12.2.121
- 511 Reiter, M., Chamberlin, R. M., & Love, D. W. (2010). New data reflect on the ther-
512 mal antiquity of the socorro magma body locale, rio grande rift, new mexico.
513 *Lithosphere*, *2*(6), 447–453. doi: 10.1130/L115.1
- 514 Rinehart, E. J., & Sanford, A. R. (1981). Upper crustal structure of the rio grande
515 rift near socorro, new mexico, from inversion of microearthquake s-wave reflec-
516 tions. *Bulletin of the Seismological Society of America*, *71*(2), 437–450. doi:
517 <https://doi.org/10.1785/BSSA0710020437>
- 518 Rivalta, E., & Segall, P. (2008). Magma compressibility and the missing source for
519 some dike intrusions. *Geophysical Research Letters*, *35*(4).

- 520 Sandwell, D., Mellors, R., Tong, X., Wei, M., & Wessel, P. (2011). Open radar inter-
 521 ferometry software for mapping surface deformation. *Eos Trans. AGU*, *92*(28),
 522 LLNL-TR-481284, 1090004. doi: 10.1029/2011EO280002
- 523 Sanford, A., Lin, K., Tsai, I., & Jacksha, L.
 524 Earthquake catalogs for new mexico and bordering areas: 1869–1998. .
- 525 Stankova, J., Bilek, S. L., Rowe, C. A., & Aster, R. C. (2008). Characteris-
 526 tics of the october 2005 microearthquake swarm and reactivation of similar
 527 event seismic swarms over decadal time periods near socorro, new mex-
 528 ico. *Bulletin of the Seismological Society of America*, *98*(1), 93–105. doi:
 529 <https://doi.org/10.1785/0120070108>
- 530 Torres, R., Snoeij, P., Geudtner, D., Bibby, D., Davidson, M., & Attema, E. e. a.
 531 (2012). Gmes sentinel-1 mission. *Remote Sensing of Environment*, *120*, 9-
 532 24. Retrieved from <https://doi.org/10.1016/j.rse.2011.05.028> doi:
 533 10.1016/j.rse.2011.05.028
- 534 Wang, X., & Aoki, Y. (2019). Post-eruptive thermoelastic deflation of intruded
 535 magma in usu volcano, japan, 1992–2017. *Journal of Geophysical Research:*
 536 *Solid Earth*, *124*(1), 335–357.
- 537 Ward, K. M., Zandt, G., Beck, S. L., Christensen, D. H., & McFarlin, H. (2014).
 538 Seismic imaging of the magmatic underpinnings beneath the altiplano-puna
 539 volcanic complex from the joint inversion of surface wave dispersion and
 540 receiver functions. *Earth and Planetary Science Letters*, *404*, 43-53. doi:
 541 10.1016/j.epsl.2014.07.022
- 542 West, M., Ni, J., Baldrige, W., Wilson, D., Aster, R., Gao, W., & Grand, S.
 543 (2004). Crust and upper mantle shear-wave structure of the southwest United
 544 States: Implications for rifting and support for high elevation. *J. Geophys.*
 545 *Res.*, *109*. doi: 10.1029/2003JB002575
- 546 Wilson, D., Aster, R., West, M., Ni, J., Grand, S., Gao, W., . . . Patel, P. (2005,
 547 FEB 24). Lithospheric structure of the rio grande rift. *Nature*, *433*(7028),
 548 851-855. doi: {10.1038/nature03297}
- 549 Xiao, R., Yu, C., Zhenhong, L., Song, C., & He, X. (2020). General survey of large-
 550 scale land subsidence by gacos-corrected insar stacking: Case study in north
 551 china plain. *Proc. IAHS*, *382*(213-218). Retrieved from [https://doi.org/](https://doi.org/10.5194/piahs-382-213-2020)
 552 [10.5194/piahs-382-213-2020](https://doi.org/10.5194/piahs-382-213-2020) doi: 10.5194/piahs-382-213-2020